

Ballistic Surfing Acceleration as a Coherent Mechanism for Electron Acceleration in Galaxy Cluster Shocks

Ji-Hoon Ha¹ and Krzysztof Stasiewicz²

¹*Korea Astronomy and Space Science Institute (KASI), Daejeon, Republic of Korea*

²*Space Research Centre, Polish Academy of Sciences, Warsaw, Poland*

Radio relics in merging galaxy clusters are widely interpreted as synchrotron emission from relativistic electrons accelerated at large-scale shocks. However, the efficiency of diffusive shock acceleration (DSA) is expected to be reduced in the low-Mach-number, weakly turbulent environments characteristic of cluster merger shocks, and recent results suggest that DSA itself may not constitute a viable physical mechanism. In this work, we investigate ballistic surfing acceleration (BSA) as an electrodynamically grounded mechanism for electron energization that does not rely on prescribed diffusion coefficients. We formulate BSA under typical cluster shock conditions and derive the balance between coherent acceleration by the shock convection electric field and radiative losses due to synchrotron and inverse-Compton cooling. This balance determines both the maximum electron energy and the resulting steady-state spectrum. By forward-modeling the associated synchrotron emission and comparing it with integrated radio observations of the Sausage and Toothbrush relics, we find that the observed spectral curvature and high-frequency steepening can be reproduced when only a very small fraction ($\sim 10^{-9} - 10^{-8}$) of the available BSA acceleration capacity contributes to systematic electron energization. Despite this extremely small efficiency, it is sufficient to accelerate electrons to Lorentz factors $\gamma \sim 10^4 - 10^5$ under cluster conditions. These results suggest that radio relics provide a promising astrophysical laboratory for probing coherent acceleration, and that the BSA framework may account for the production of relativistic electrons in cluster shocks.

I. INTRODUCTION

Radio relics are large-scale, diffuse synchrotron sources observed predominantly in the peripheral regions of merging galaxy clusters [e.g., 1–6, and references therein]. They are typically elongated, highly polarized, and characterized by steep radio spectra, strongly suggesting an origin associated with merger-driven shock waves propagating through the intracluster medium (ICM). The relativistic electrons responsible for the observed synchrotron emission are generally inferred to have Lorentz factors of order $\gamma \sim 10^4 - 10^5$ [e.g., 7–9].

The standard theoretical framework employed to interpret radio relics is diffusive shock acceleration (DSA) [e.g., 10–12], in which particles gain energy through repeated shock crossings mediated by scattering off magnetic turbulence. Within this paradigm, the observed radio spectral index is commonly used to infer the shock Mach number. However, the application of DSA to galaxy cluster merger shocks remains an active area of investigation. Cluster shocks are typically characterized by low Mach numbers ($\mathcal{M} \lesssim 3$), weak magnetic fields, and uncertain levels of turbulence—conditions under which efficient electron injection and acceleration may be more difficult to achieve. Semi-analytic and numerical studies suggest that the acceleration efficiency decreases toward lower Mach numbers in this regime [e.g., 13–17], although the extent of this reduction continues to be explored. In addition, DSA models often rely on parameterized descriptions of particle diffusion and pitch-angle scattering whose microphysical origins are still being investigated, particularly in the tenuous intracluster medium (ICM).

Several physical mechanisms have been proposed to improve electron acceleration at weak cluster shocks

within the broader diffusive framework. One possibility is that pre-existing turbulence in the upstream medium enhances particle scattering, effectively increasing the residence time near the shock and facilitating more efficient energization. Recent studies suggest that externally driven or inherited turbulence can, in principle, lower the effective injection threshold and modify the spectral properties of accelerated particles, although the required turbulence levels and coherence scales remain uncertain in the intracluster medium [e.g., 18, 19]. Another widely discussed scenario involves the re-acceleration of pre-existing suprathermal or fossil electron populations, which can partially bypass the injection barrier and produce observable radio emission even at low Mach numbers [e.g., 4, 9, 20, 21]. These scenarios highlight the diversity of pathways through which relativistic electrons may be generated in cluster environments. At the same time, such mechanisms depend on environmental factors—including the level of upstream turbulence and the availability of nonthermal seed particles—that are expected to vary across clusters and merger histories. For example, radio relics are predominantly located in the outskirts of merging systems, where the number density of active galactic nuclei may be lower than in cluster cores [e.g., 22], potentially influencing the supply of fossil electrons. Taken together, these considerations point toward a complex acceleration landscape in which multiple processes may contribute, motivating the exploration of alternative channels that could replace diffusive acceleration mechanisms in galaxy cluster shocks.

Diffusion, whether occurring in velocity space and/or in configuration space, is a relaxation process that drives the distribution function toward equilibrium and does not necessarily lead to systematic particle energization.

In contrast, ballistic surfing acceleration (BSA) [23], which arises naturally from the presence of magnetic-field gradients in collisionless shocks, provides a direct acceleration mechanism for particles whose gyroradii exceed the width of the magnetic ramp in a shock. In this framework, particle energization results from work done by the convection electric field generated by plasma flow across the magnetic field, as observed in the shock reference frame. Particles gain more energy in the upstream region than they lose in the downstream region, leading to systematic acceleration when averaged over a gyroperiod. Processes occurring within the shock ramp — such as resonant wave–particle interactions or turbulent diffusion — do not contribute significantly to the acceleration of high-energy particles gyrating across the shock, but instead act primarily to isotropize their distribution.

A key feature of BSA is its strong dependence on shock geometry: the acceleration efficiency is expected to be highest at perpendicular shocks, where the motional electric field reaches its maximum amplitude, and to decrease toward the parallel limit. Importantly, cosmological simulations of large-scale structure formation suggest that quasi-perpendicular shocks are common, accounting for roughly $\sim 70\%$ of merger-driven and cosmological shocks [e.g., 24–26]. This trend has been reported both in large cosmological volumes and in cluster-focused simulations designed to reproduce radio relic environments, which similarly find that relic-hosting shocks are frequently quasi-perpendicular [e.g., 27]. Consequently, the geometric conditions favorable for BSA appear to be widespread in galaxy cluster merger shocks.

In this paper, we investigate whether BSA can operate efficiently in galaxy cluster merger shocks and contribute to the relativistic electron populations responsible for radio relic emission. Focusing on typical cluster shock conditions, we examine the balance between BSA-driven acceleration and radiative energy losses, derive the corresponding maximum electron energies and steady-state spectra, and compare the resulting predictions with the observed radio spectral properties of representative cluster relics.

II. BALLISTIC SURFING ACCELERATION: PHYSICAL PICTURE

Ballistic surfing acceleration (BSA) [23] is a particle acceleration mechanism that follows directly from the electrodynamics of collisionless shocks. The physical basis of BSA can be understood from the relativistic momentum equation for electrons with charge e , rest mass m_e , and velocity \mathbf{v} in electromagnetic fields \mathbf{E} and \mathbf{B} :

$$\frac{d\mathbf{p}}{dt} = e \left(\mathbf{E} + \frac{\mathbf{v}}{c} \times \mathbf{B} \right), \quad (1)$$

where $\mathbf{p} = \gamma m_e \mathbf{v}$, $\gamma = (1 - v^2/c^2)^{-1/2}$, and c is the speed of light. This implies that the kinetic energy gain of a

particle is entirely due to the electric field,

$$\Delta K = e \int \mathbf{E} \cdot \mathbf{v} dt, \quad (2)$$

where $K \equiv (m_e^2 c^4 + p^2 c^2)^{1/2} - m_e c^2$.

In general, there are three types of electric fields that determine particle dynamics and energization processes in the shock frame: $\mathbf{E}_{\text{conv}} = -\mathbf{V} \times \mathbf{B}/c$ — the convection electric field; $\hat{\mathbf{x}} E_S(x)$ — the cross-shock electric field, maintained by the electron pressure gradient and directed along the shock normal $\hat{\mathbf{x}}$ aligned with the bulk velocity \mathbf{V} ; and $\tilde{\mathbf{E}}(\mathbf{r}, t)$ — the wave electric field of arbitrary modes. The convection electric field is $E_{\text{conv}} = (V_u/c) B_u \sin \zeta$, where the subscript ‘u’ refers to upstream values and ζ is the shock angle.

Thermal particles are rapidly accelerated by strong wave electric fields $\tilde{E} \lesssim 100 \text{ mVm}^{-1}$ observed in the bow shock, via the stochastic wave energization (SWE) mechanism [28–30]. Once their gyroradius, r_c , exceeds the shock width ($r_c > \Delta$), BSA becomes the dominant acceleration mechanism.

High-energy particles with gyroradii much larger than the width of the shock (typically of the order of the thermal proton gyroradius) spend a negligible fraction of a gyroperiod inside the ramp. Therefore, acceleration by the fields $\mathbf{E} = \mathbf{E}_{\text{conv}} + \hat{\mathbf{x}} E_S + \tilde{\mathbf{E}}$ inside the shock is negligible in comparison to acceleration by \mathbf{E}_{conv} outside the shock.

In this framework, the energization of high-energy particles is governed by their interaction with the large-scale electric field \mathbf{E}_{conv} (constant across the shock in the one-dimensional approximation), rather than by stochastic scattering off magnetic turbulence and repeated shock crossings. This acceleration occurs during “surfing” outside the shock ramp, in a region where magnetic-field gradients and wave activity are weak. As a result, acceleration by waves, $e \int \tilde{\mathbf{E}} \cdot \mathbf{v} dt$, averages to zero outside the shock, while ∇B drifts do not occur. Consequently, BSA is conceptually distinct from shock drift acceleration (SDA) [e.g., 31–33], which relies on ∇B drifts within the shock transition, applies mostly to low-energy particles ($r_c < \Delta$), and is equivalent to quasi-adiabatic heating (QAH) [28].

The efficiency of BSA depends sensitively on the shock geometry. In quasi-perpendicular shocks, where the convection electric field is maximized, particles gain more energy during surfing in the low upstream magnetic field B_u than they lose while gyrating in the compressed downstream field B_d , as clearly illustrated in Fig. 3 of Ref. [23]. In contrast, for parallel shocks the convection electric field vanishes, and ballistic surfing acceleration becomes ineffective. This strong dependence on shock obliquity is a defining feature of the BSA mechanism and leads to acceleration efficiencies that vary continuously with shock angle.

Originally developed to explain cosmic-ray acceleration and validated using high-resolution measurements at the Earth’s bow shock, ballistic surfing acceleration provides

a physically transparent description of particle energization in collisionless shocks. The essential ingredients of the mechanism are the large-scale convection electric field and the magnetic-field ramp, while pitch-angle scattering is required only to keep particles in the vicinity of the shock and to facilitate repeated gyrations around the magnetic ramp.

Below, we apply the BSA model to galaxy cluster merger shocks, which are typically non-relativistic, weakly magnetized, and characterized by low Mach numbers. The energy gain per gyroperiod, averaged over an initially isotropic distribution function, is given by Eq. (4) in Ref. [23] and reads

$$\Delta K \approx g(1 - c_B^{-1}) \frac{E_{\text{conv}}}{B_u} K, \quad (3)$$

where $c_B = B_d/B_u$ is the shock compression ratio, and $g \lesssim 1$ is a geometric factor that depends on the shock angle, attaining its maximum value for perpendicular shocks. The observed spectrum of cosmic rays is consistent with $g \approx 0.8$ as shown in Ref. [23].

Using Eq. (3) for relativistic electrons with kinetic energy $K \approx \gamma m_e c^2$, and gyrofrequency $\omega_c = eB/\gamma m_e c$, the energy gain rate per gyroperiod can be expressed in terms of the relativistic Lorentz factor as

$$\dot{\gamma}_{\text{BSA}} = \eta \frac{eE_{\text{conv}}}{m_e c}, \quad \eta \equiv \frac{g}{\pi} \frac{(1 - c_B^{-1})}{(1 + c_B^{-1})}. \quad (4)$$

For typical galaxy cluster shocks with $c_B \sim 2-3$, $\eta \sim 0.1$.

Eq. (4) represents the BSA acceleration capacity for particles with cyclotron orbits that actually cross the shock. However, such particles constitute only a small (and generally unknown) fraction of the electron population present in galaxy cluster shocks. We therefore introduce an efficiency parameter $\eta_{\text{BSA}} \ll 1$ and define an acceleration rate, averaged over the entire source region, as

$$\dot{\gamma}_{\text{acc}} \approx \eta_{\text{BSA}} \dot{\gamma}_{\text{BSA}}. \quad (5)$$

The radio relic spectra modeled in this work constrain the efficiency to small values of η_{BSA} , thereby quantifying the net, time-averaged energization relative to the intrinsic BSA rate. They do not imply weak microscopic acceleration, but instead reflect the reduction from the ideal coherent-surfing limit to the ensemble-averaged acceleration expected once finite trapping times, shock geometry, and unresolved kinetic-scale transport are taken into account.

Several important features of the acceleration rate follow immediately from this formulation. First, the acceleration rate is independent of particle energy, implying linear energy growth in time in the absence of losses. Second, the acceleration efficiency depends explicitly on the shock obliquity through the geometric factor g and E_{conv} . It vanishes in the limit of parallel shocks, where the motional electric field disappears, and also in the absence of shocks, when $c_B = 1$. Finally, the acceleration

rate depends only on macroscopic shock parameters and does not invoke particle diffusion coefficients or turbulent scattering rates.

This description is therefore well suited for application to galaxy cluster merger shocks, where large-scale electrodynamic fields are robustly present while the microphysics of particle scattering remains uncertain. In the following sections, this acceleration rate is combined with radiative loss processes to determine the maximum electron energy and the resulting steady-state electron spectrum.

III. GALAXY CLUSTER MERGER SHOCK ENVIRONMENT

Galaxy cluster merger shocks propagate through the intracluster medium, a hot, dilute plasma characterized by temperatures of several keV [e.g., 34, 35] and particle densities of order 10^{-4} – 10^{-3} cm $^{-3}$ [e.g., 36]. Observations indicate that typical shock velocities range from a few hundred to approximately 10 3 km s $^{-1}$ [e.g., 37], while magnetic field strengths in the cluster outskirts are commonly estimated to be of order μ G or lower [e.g., 2, 38]. These conditions correspond to non-relativistic shocks with small Mach numbers [e.g., 39–42].

Compared to supernova remnant shocks, cluster merger shocks are typically weaker and evolve over much larger spatial and temporal scales. These differences provide an opportunity to examine how particle acceleration operates across markedly different shock environments. In such regimes, the relative importance of various acceleration processes may differ from that in supernova remnants, reflecting the lower Mach numbers and extended dynamical timescales of cluster shocks. At the same time, the large shock surfaces and long lifetimes imply that even modest acceleration efficiencies can lead to observable nonthermal signatures.

For relativistic electrons in the intracluster medium, radiative energy losses play a central role in determining the shape and extent of the particle energy distribution. The dominant loss processes are synchrotron radiation in the cluster magnetic field and inverse-Compton scattering off cosmic microwave background (CMB) photons [e.g., 43, 44]. Both processes arise from interactions between relativistic electrons and ambient electromagnetic fields and lead to continuous energy losses that scale quadratically with the electron Lorentz factor [e.g., 45]. The total radiative energy loss rate can be written as

$$\dot{\gamma}_{\text{loss}} = -\frac{4}{3} \frac{\sigma_T c}{m_e c^2} (U_B + U_{\text{CMB}}) \gamma^2, \quad (6)$$

where σ_T is the Thomson cross section. The quantity U_B denotes the magnetic field energy density associated with synchrotron losses, while U_{CMB} represents the energy density of the cosmic microwave background radiation responsible for inverse-Compton cooling. The mag-

netic energy density is given by

$$U_B = \frac{B^2}{8\pi}, \quad (7)$$

where B is the local magnetic field strength, while the CMB energy density evolves with redshift as

$$U_{\text{CMB}} = U_{\text{CMB},0} (1+z)^4, \quad (8)$$

with $U_{\text{CMB},0}$ denoting the present-day CMB energy density.

Eq. (6) follows from classical electrodynamics in the Thomson regime and applies as long as the electron energies relevant for radio synchrotron emission satisfy $\gamma h\nu_{\text{CMB}} \ll m_e c^2$, a condition well satisfied for cluster radio relic electrons. The quadratic dependence on γ reflects the fact that both synchrotron and inverse-Compton losses scale with the square of the electron energy.

In galaxy clusters, the relative importance of synchrotron and inverse-Compton losses is determined by the ratio U_B/U_{CMB} . For typical magnetic field strengths of $0.1 - 1 \mu\text{G}$ in cluster outskirts, the magnetic energy density is often comparable to or smaller than the CMB energy density, particularly at moderate redshifts [44]. As a result, inverse-Compton cooling frequently dominates the total radiative losses of relativistic electrons in radio relics.

In principle, radiative losses depend on the total electromagnetic acceleration experienced by a charged particle. One may therefore ask whether the convection electric field associated with the shock contributes an additional radiative loss term. For cluster merger shocks, however, the convection electric field satisfies $E_{\text{conv}} = (V_u/c)B_u$, where the upstream velocity V_u is much smaller than the speed of light. As a result, the radiative contribution associated with E_{conv} is suppressed relative to the magnetic-field-driven transverse acceleration by a factor of order $(V_u/c)^2$. The standard synchrotron loss expression therefore provides an excellent approximation under intracluster conditions.

Any viable acceleration mechanism operating in cluster merger shocks must therefore compete effectively with these radiative losses in order to sustain electrons at Lorentz factors $\gamma \sim 10^4 - 10^5$ required for observable radio synchrotron emission [e.g., 7–9]. In the following section, we combine the acceleration rate derived for BSA with the loss rate given above to determine the maximum electron energy attainable in cluster shocks.

IV. MAXIMUM ELECTRON ENERGY FROM ACCELERATION–LOSS BALANCE

The maximum energy attainable by electrons accelerated via ballistic surfing acceleration is determined by the competition between systematic energy gain and radiative losses. In the steady-state limit, the highest electron

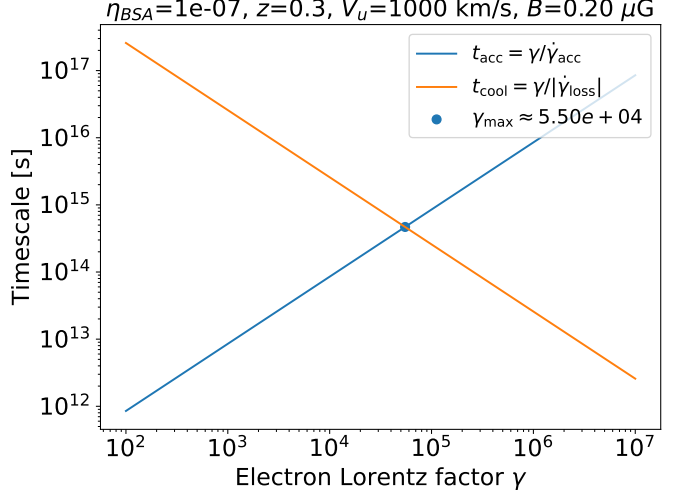


FIG. 1. Comparison between the acceleration timescale $t_{\text{acc}} = \gamma/\dot{\gamma}_{\text{acc}}$ and the radiative cooling timescale $t_{\text{cool}} = \gamma/|\dot{\gamma}_{\text{loss}}|$ as functions of the electron Lorentz factor for representative cluster merger shock parameters. The intersection of the two curves defines the maximum attainable Lorentz factor γ_{max} , illustrating that the high-energy cutoff arises naturally from the balance between ballistic surfing acceleration and radiative losses.

energy is reached when the acceleration timescale equals the radiative cooling timescale, corresponding to a balance between energy gain and loss rates.

This condition provides a direct and physically transparent estimate of the maximum electron Lorentz factor attainable in galaxy cluster merger shocks. Importantly, the resulting expression depends only on macroscopic shock properties—such as the upstream flow velocity, magnetic field strength, and redshift—together with an effective efficiency parameter describing the ballistic surfing process. No assumptions regarding particle diffusion coefficients or turbulent scattering rates are required.

A. Acceleration–Cooling Balance and Maximum Lorentz Factor

The balance condition can be expressed as

$$\dot{\gamma}_{\text{acc}} + \dot{\gamma}_{\text{loss}} = 0, \quad (9)$$

where $\dot{\gamma}_{\text{acc}}$ is the acceleration rate associated with ballistic surfing and $\dot{\gamma}_{\text{loss}}$ is the combined synchrotron and inverse-Compton loss rate. Substituting Eqs. (4) and (6), the maximum electron Lorentz factor is given by

$$\gamma_{\text{max}} \simeq \left[\frac{3 \eta \eta_{\text{BSA}} e E_{\text{conv}}}{4 \sigma_T (U_B + U_{\text{CMB}})} \right]^{1/2}. \quad (10)$$

The physical meaning of this balance is illustrated in Fig. 1, which compares the acceleration timescale $t_{\text{acc}} = \gamma/\dot{\gamma}_{\text{acc}}$ and the radiative cooling timescale $t_{\text{cool}} =$

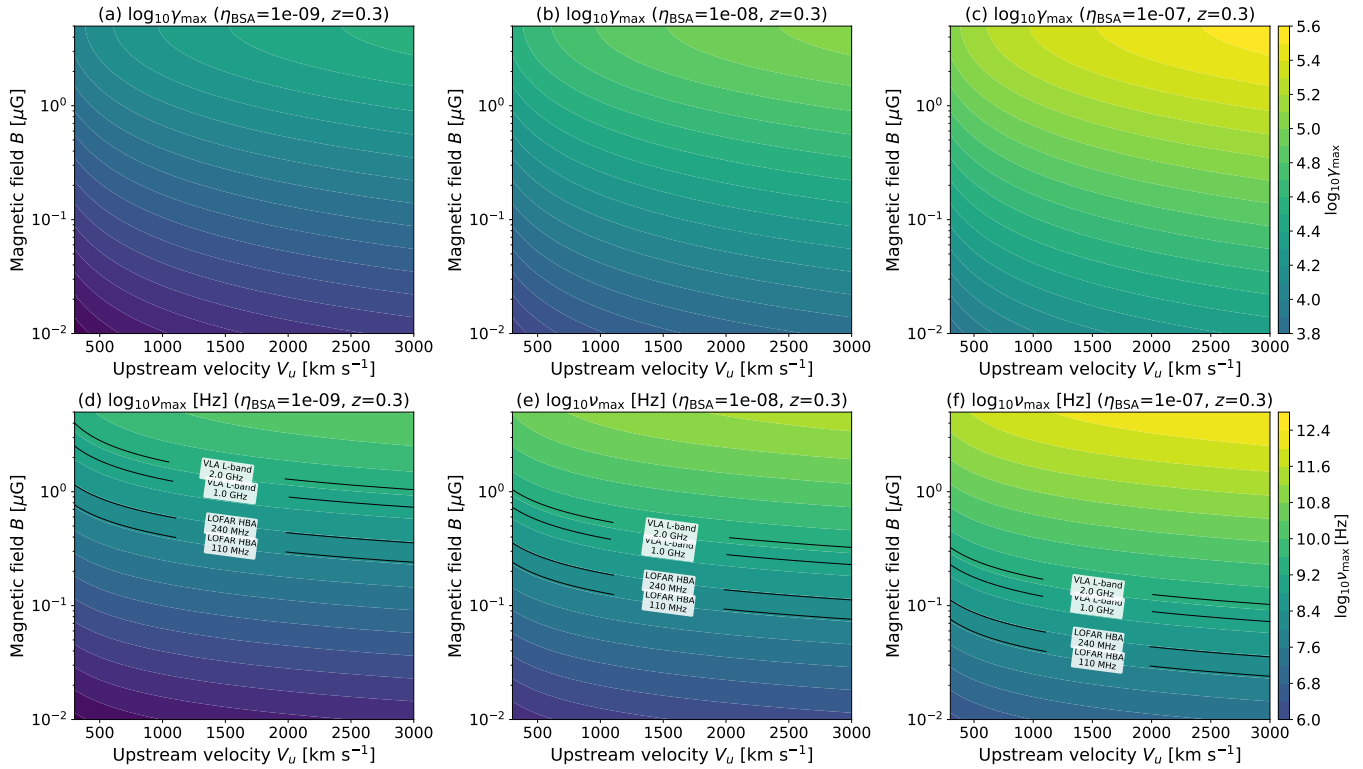


FIG. 2. Mapping between ballistic surfing acceleration and observable radio emission in galaxy cluster merger shocks. The upper panels show the maximum electron Lorentz factor γ_{\max} , determined by the balance between BSA and radiative losses, as a function of upstream velocity V_u and magnetic field strength B for two representative values of η_{BSA} . The lower panels show the corresponding maximum synchrotron frequency ν_{\max} inferred from γ_{\max} , with the characteristic observing bands of LOFAR (HBA) [46] and the VLA (L-band) [47] indicated.

$\gamma/|\dot{\gamma}_{\text{loss}}|$ as functions of electron energy. The intersection of the two curves directly defines γ_{\max} , demonstrating that the maximum electron energy arises naturally from the competition between coherent electrodynamic acceleration and radiative losses.

B. From Maximum Electron Energy to Observable Radio Frequencies

While Eq. (10) characterizes the efficiency of ballistic surfing acceleration in terms of particle energy, radio relics are observed through their synchrotron emission at specific frequencies. A direct comparison with observations therefore requires translating the maximum electron Lorentz factor into the corresponding characteristic synchrotron frequency.

For relativistic electrons emitting in a magnetic field B , the characteristic synchrotron frequency is given by

$$\nu_c \simeq \frac{3eB}{4\pi m_e c} \gamma^2. \quad (11)$$

This relation establishes a direct mapping between the particle energy space and observable radio frequencies.

In Fig. 2, we evaluate Eq. (10) over a broad range of representative cluster merger shock parameters and

show both the resulting maximum electron Lorentz factor γ_{\max} and the corresponding maximum synchrotron frequency ν_{\max} . The figure delineates the regions of parameter space in which ballistic surfing acceleration can produce electrons energetic enough to account for observed radio relic emission at commonly probed frequencies. In the cluster outskirts, radiative losses of relativistic electrons are dominated by inverse-Compton (IC) scattering off the cosmic microwave background (CMB), because U_{CMB} typically exceeds the magnetic energy density $U_B = B^2/8\pi$ for μG -level fields. In this IC-dominated regime, the cooling rate is well approximated by $\dot{\gamma}_{\text{loss}} \approx -(4/3)(\sigma_T c/m_e c^2) U_{\text{CMB}} \gamma^2$, so that the cooling timescale scales as $t_{\text{cool}} \propto \gamma^{-1}$ and is only weakly sensitive to B . In contrast, BSA is driven by the large-scale convective electric field upstream of the shock, $E_{\text{conv}} = V_u B/c$, yielding an approximately energy-independent acceleration rate $\dot{\gamma}_{\text{acc}} \propto \eta_{\text{BSA}} E_{\text{conv}} \propto \eta_{\text{BSA}} V_u B$. Therefore, increasing B enhances the acceleration efficiency and shifts the acceleration-loss balance to higher energies, implying a larger γ_{\max} for stronger magnetic fields.

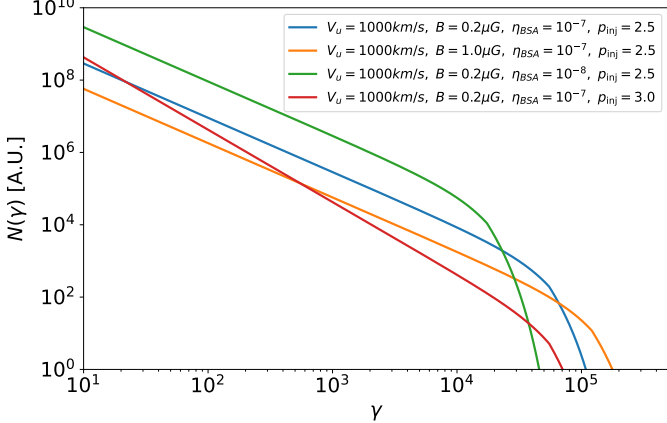


FIG. 3. Steady-state electron energy distributions $N(\gamma)$ produced by ballistic surfing acceleration in galaxy cluster merger shocks. Different curves illustrate the dependence on magnetic field strength, BSA efficiency, and injection spectral index, while the high-energy steepening near γ_{\max} reflects radiative cooling.

V. STEADY-STATE ELECTRON SPECTRUM AND SYNCHROTRON EMISSION

A. Steady-State Electron Spectrum

Beyond estimating the maximum electron energy, a meaningful comparison with radio relic observations requires modeling the steady-state energy distribution of relativistic electrons established by the interplay between acceleration, injection, and radiative losses. To this end, we consider a simplified transport equation describing the evolution of the electron distribution function $N(\gamma)$ in energy space.

The electron population is governed by the kinetic equation

$$\frac{d}{d\gamma} [(\dot{\gamma}_{\text{acc}} + \dot{\gamma}_{\text{loss}}) N(\gamma)] + \frac{N(\gamma)}{t_{\text{esc}}} = Q(\gamma), \quad (12)$$

In solving Eq. (12), we adopt a power-law injection term, $Q(\gamma) = Q_0 \gamma^{-q_{\text{inj}}}$ for $\gamma \geq \gamma_{\text{inj,min}}$, where $\gamma_{\text{inj,min}}$ represents the minimum Lorentz factor of seed electrons. For a meaningful comparison across different shock and magnetic-field parameters, the normalization Q_0 is not kept fixed; instead, it is determined by requiring a fixed *injected energy rate* into relativistic electrons,

$$\dot{K}_{\text{inj}} \propto \int_{\gamma_{\text{inj,min}}}^{\gamma_{\text{max}}} \gamma Q(\gamma) d\gamma = \text{const.} \quad (13)$$

This choice ensures that differences among the steady-state solutions arise from the competition between ballistic surfing acceleration and radiative losses (through the parameter-dependent γ_{max}), rather than from an arbitrary change in the overall injection power. Solving Eq. (12) in the cooling-dominated regime then yields

the steady-state electron energy distributions shown in Fig. 3. We observed that the trend shown in Fig. 3 is fully consistent with the $\gamma_{\max}(V_u, B)$ maps in Fig. 2.

We also note that particle escape does not control the high-energy spectrum in the relic environment. The characteristic radiative cooling time for electrons emitting at radio frequencies ($\gamma \sim 10^4$ – 10^5) is typically much shorter than the macroscopic advection or leakage time across the acceleration region, which is of order $t_{\text{esc}} \sim L/V_u$ for a region of size L . Given the large spatial scales of cluster merger shocks and relic widths ($L \sim 10^2$ kpc) and shock speeds of $V_u \sim 10^3$ km s $^{-1}$, one expects $t_{\text{esc}} \sim 10^2$ Myr to be significantly longer than both $t_{\text{cool}} \sim 10$ Myr and the effective acceleration time $t_{\text{acc}} \sim 10$ Myr over the energies of interest (e.g., $\gamma \sim 10^4$ – 10^5).

B. Synchrotron Emission from BSA-Accelerated Electrons

Using the steady-state electron distributions derived in Section V A, we compute the resulting synchrotron emission by forward modeling the radiative output of relativistic electrons in the intracluster magnetic field. For a given isotropic electron distribution $N(\gamma)$, the synchrotron emissivity per unit frequency in the emitting frame is written as

$$j_{\nu, \text{em}} = \int_{\gamma_{\min}}^{\gamma_{\max}} N(\gamma) P_{\text{syn}}(\nu_{\text{em}}, \gamma) d\gamma, \quad (14)$$

where $P_{\text{syn}}(\nu, \gamma)$ is the single-electron synchrotron power per unit frequency and $\nu_{\text{em}} = (1+z)\nu_{\text{obs}}$ accounts for cosmological redshift. For an isotropic pitch-angle distribution, the single-electron synchrotron power is

$$P_{\text{syn}}(\nu, \gamma) = \frac{\sqrt{3} e^3 B}{m_e c^2} F\left(\frac{\nu}{\nu_c}\right), \quad \nu_c = \frac{3eB}{4\pi m_e c} \gamma^2, \quad (15)$$

where $F(x) = x \int_x^\infty K_{5/3}(\xi) d\xi$ is the standard synchrotron kernel and $K_{5/3}$ denotes the modified Bessel function of the second kind. This formulation maps the electron energy distribution directly into an observable radio spectrum without invoking a phenomenological power-law prescription.

To relate the BSA-driven acceleration spectrum to the emitting electron population, we assume that BSA operates primarily in the upstream region and within the shock transition layer, where electrons are energized up to a maximum Lorentz factor γ_{\max} set by the balance between coherent acceleration and radiative losses. Upon crossing the shock, this accelerated population is injected into the downstream flow with the cutoff distribution described below. Subsequent evolution is assumed to be governed by radiative cooling and advection, while any additional downstream acceleration is neglected.

Under these assumptions, we compute the electron distribution in the emission region by solving the steady-state transport equation including radiative cooling and

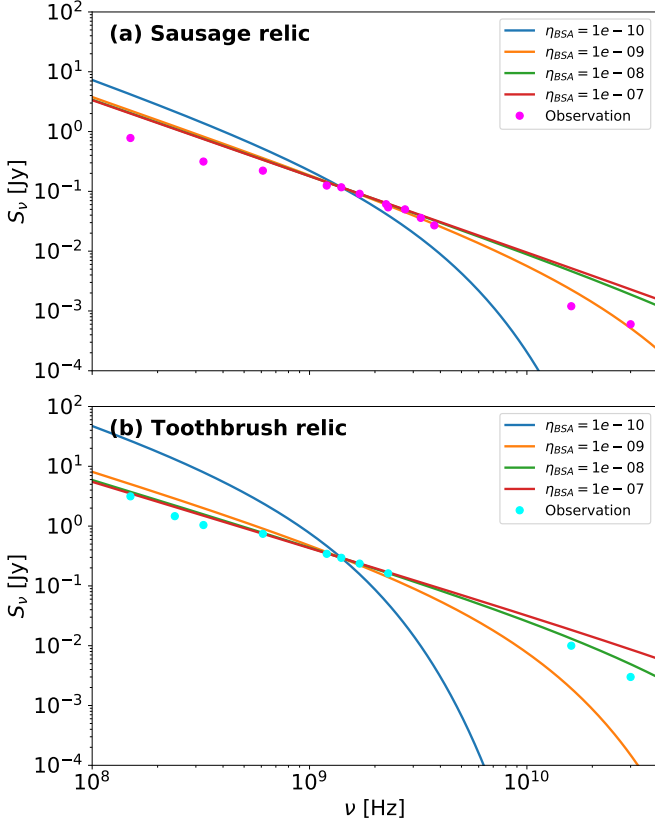


FIG. 4. Synchrotron spectra produced by BSA-accelerated electrons in galaxy cluster shocks, compared with integrated radio relic observations. The upper and lower panels show the Sausage and Toothbrush relics, respectively. Solid curves denote model spectra for different values of the BSA efficiency parameter η_{BSA} , while points indicate observed integrated flux densities [3].

particle escape,

$$\frac{d}{d\gamma} (\dot{\gamma}_{\text{loss}} N(\gamma)) + \frac{N(\gamma)}{t_{\text{esc}}} \approx Q(\gamma), \quad (16)$$

where $Q(\gamma)$ denotes the injected electron spectrum, t_{esc} is the characteristic escape (or advection) timescale from the emission region, and the radiative energy loss rate is $\dot{\gamma}_{\text{loss}} = -a_{\text{loss}}\gamma^2$, with

$$a_{\text{loss}} = \frac{4}{3} \frac{\sigma_T c}{m_e c^2} (U_B + U_{\text{CMB}}). \quad (17)$$

The resulting solution can be written as

$$N(\gamma) \approx \frac{1}{|\dot{\gamma}_{\text{loss}}|} \int_{\gamma}^{\infty} Q(\gamma') \exp \left[- \int_{\gamma}^{\gamma'} \frac{d\tilde{\gamma}}{|\dot{\gamma}_{\text{loss}}(\tilde{\gamma})| t_{\text{esc}}} \right] d\gamma', \quad (18)$$

which describes an electron population shaped by the combined effects of radiative cooling and finite residence time downstream of the shock. In Eq. (18), the injected electron spectrum $Q(\gamma)$ is assumed to follow a power-law

form,

$$Q(\gamma) \propto \gamma^{-p_{\text{inj}}} \exp \left(-\frac{\gamma}{\gamma_{\text{max}}} \right), \quad (19)$$

where the maximum Lorentz factor γ_{max} is determined by the balance between BSA and radiative losses.

The observed flux-density spectrum is obtained from the emitted spectrum by accounting for cosmological redshift. For a direct comparison of spectral shapes, each model spectrum is normalized to match the observed flux density at a reference frequency $\nu_0 = 1.4 \text{ GHz}$,

$$S_{\nu}^{\text{model}}(\nu) \approx j_{\nu}(\nu) \frac{S_{\nu, \text{obs}}(\nu_0)}{j_{\nu}(\nu_0)}. \quad (20)$$

This procedure isolates the spectral curvature and high-frequency rollover introduced by ballistic surfing acceleration and radiative cooling, without introducing additional free parameters associated with the emitting volume or source distance.

Fig. 4 shows the resulting synchrotron spectra for several values of the effective BSA efficiency parameter η_{BSA} , compared with integrated flux-density measurements of the Sausage and Toothbrush relics. We find that values $\eta_{\text{BSA}} \sim 10^{-9}-10^{-8}$ reproduce the observed spectral curvature and high-frequency steepening most consistently. Larger values lead to excessively hard spectra owing to unrealistically large maximum electron energies, whereas smaller values fail to accelerate electrons to Lorentz factors required for GHz-frequency synchrotron emission. The observed relic spectra therefore constrain the effective, time-averaged energization rate to a relatively narrow range set by the balance between coherent electrodynamic acceleration and radiative losses.

The small values of η_{BSA} should not be interpreted as a weakness of the underlying electrodynamic acceleration mechanism. Rather, η_{BSA} characterizes the net, ensemble-averaged energization experienced by electrons in realistic cluster merger shocks, where sustained coherent acceleration is expected to be limited by finite upstream residence times, orbit decoherence, and the restricted range of particle trajectories that satisfy the geometric conditions for ballistic surfing. These macroscopic transport effects naturally reduce the time-averaged acceleration relative to the idealized rate without requiring fine tuning.

Despite this strong reduction, the inferred efficiency remains sufficient to accelerate electrons to Lorentz factors $\gamma \sim 10^4-10^5$ in the intracluster medium, owing to the energy-independent acceleration rate of BSA and the dominance of inverse-Compton cooling. The resulting spectra are reproduced in a physically self-consistent manner, indicating that BSA can provide a viable channel for generating relativistic electrons in cluster merger shocks. More broadly, these results suggest that coherent electrodynamic processes may contribute to shaping the nonthermal electron population in radio relics. Whether such processes operate independently or in combination

with other proposed acceleration mechanisms remains an open question that warrants further investigation.

C. Injection Constraint and Energetic Viability of Ballistic Surfing Acceleration

A useful measure of the global impact of BSA is obtained by linking particle-level energization to the macroscopic energy budget of the shock. The instantaneous energy gain of a single electron is $\dot{K}(\gamma) = m_e c^2 \dot{\gamma}_{\text{acc}}$, where $\dot{\gamma}_{\text{acc}} \approx \eta_{\text{BSA}} \dot{\gamma}_{\text{BSA}}$. For a relativistic electron population described by the distribution $N(\gamma)$ within the energization region, the volumetric power deposited into electrons can be written as

$$\dot{U}_e^{(\text{BSA})} = \int_{\gamma_{\text{min}}}^{\gamma_{\text{max}}} N(\gamma) m_e c^2 \dot{\gamma}_{\text{acc}} d\gamma = m_e c^2 \dot{\gamma}_{\text{acc}} n_{e,\text{inj}}, \quad (21)$$

where $n_{e,\text{inj}} \equiv \int N(\gamma) d\gamma$ is the number density of accelerated electrons. The associated energy flux can be estimated as $F_e^{(\text{BSA})} \sim \dot{U}_e^{(\text{BSA})} L$, where L characterizes the effective residence scale. Comparing this with the shock kinetic energy flux $F_{\text{kin}} = \frac{1}{2} \rho V_u^3$ yields a global acceleration efficiency

$$\xi_e \equiv \frac{F_e^{(\text{BSA})}}{F_{\text{kin}}} \sim \frac{m_e c^2 \eta_{\text{BSA}} \dot{\gamma}_{\text{acc}} n_{e,\text{inj}} L}{\frac{1}{2} \rho V_u^3}, \quad (22)$$

providing a direct connection between coherent electrodynamic energization and the shock energy reservoir.

The parameter $n_{e,\text{inj}}$ can be physically interpreted through an injection fraction, $f_{e,\text{inj}} \equiv n_{e,\text{inj}}/n_e$. BSA requires that electrons possess gyroradii exceeding the thickness of the shock transition layer. In collisionless shocks, the ramp width is typically comparable to a few thermal proton gyroradii, implying that the majority of thermal electrons remain magnetically tied to the shock and do not undergo coherent surfing. Consequently, only electrons belonging to the suprathermal tail of the distribution satisfy the geometric condition $r_c > \Delta$ and can experience sustained electrodynamic acceleration. This requirement naturally introduces an injection barrier, indicating that BSA is intrinsically injection-limited. The global electron energy flux therefore scales with the product $f_{e,\text{inj}} \eta_{\text{BSA}}$, reflecting both the fraction of electrons that participate in surfing and the efficiency with which those electrons are energized.

For representative cluster merger shock parameters ($V_u \sim 10^3 \text{ km s}^{-1}$, $n \sim 10^{-4} \text{ cm}^{-3}$, $B \sim 1 \mu\text{G}$, and $L \sim 100 \text{ kpc}$), the resulting kinetic energy flux is $F_{\text{kin}} \sim 10^{-4} \text{ erg cm}^{-2} \text{ s}^{-1}$. For a characteristic shock surface of order $\sim \text{Mpc}^2$, this implies a total kinetic power of $\sim 10^{45} \text{ erg s}^{-1}$. Using these parameters, Eq. (22) can be written in a convenient normalized form as

$$\xi_e \approx 2.8 \times 10^{-4} \left(\frac{f_{e,\text{inj}}}{10^{-9}} \right) \left(\frac{\eta_{\text{BSA}}}{10^{-9}} \right). \quad (23)$$

Adopting a physically motivated, geometrically constrained injection fraction from the thermal Maxwellian electron distribution, $f_{e,\text{inj}} \sim 10^{-9}$, together with $\eta_{\text{BSA}} \sim 10^{-9}-10^{-8}$ yields a global acceleration efficiency $\xi_e \sim 10^{-4}-10^{-3}$, comfortably within the energy budget of cluster merger shocks. Such a small injection fraction is naturally expected if only electrons with gyroradii exceeding the shock thickness can undergo sustained surfing. These considerations indicate that the small electrodynamic efficiency inferred from radio spectra is fully compatible with macroscopic energetics once the injection constraint is taken into account.

D. Consistency with Inverse-Compton Constraints

The same population of relativistic electrons responsible for the synchrotron emission in radio relics must also upscatter CMB photons via IC scattering. Any viable acceleration scenario must therefore remain consistent with existing X-ray constraints.

In the Thomson regime relevant for relic electrons with Lorentz factors $\gamma \sim 10^4-10^5$, the ratio of IC to synchrotron power is approximately

$$\frac{P_{\text{IC}}}{P_{\text{syn}}} \simeq \frac{U_{\text{CMB}}}{U_B} = \left(\frac{B_{\text{CMB}}}{B} \right)^2, \quad (24)$$

where U_{CMB} and U_B are the energy densities of the CMB radiation field and the magnetic field, respectively, and $B_{\text{CMB}} \approx 3.25(1+z)^2 \mu\text{G}$ is the equivalent magnetic field strength of the CMB. For a representative redshift $z = 0.3$, this yields $B_{\text{CMB}} \simeq 5.5 \mu\text{G}$, indicating that inverse-Compton cooling dominates over synchrotron losses throughout much of the cluster outskirts parameter space considered here.

Electrons producing GHz-frequency synchrotron emission are expected to generate IC photons primarily in the hard X-ray band. To obtain an order-of-magnitude estimate of the associated flux, we map the synchrotron energy flux νS_ν produced by electrons of a given Lorentz factor to the corresponding IC energy flux via

$$E_{\text{IC}}(E) \simeq \left(\frac{U_{\text{CMB}}}{U_B} \right) \nu S_\nu. \quad (25)$$

To compare with observational limits reported in the soft X-ray band inferred from Suzaku observations of the Toothbrush relic region in the 0.3–10 keV band [e.g., 48], we estimate the band-integrated IC flux in 0.3–10 keV. In the Thomson regime, IC photons of energy E_{IC} are produced mainly by electrons with Lorentz factor

$$E_{\text{IC}} \simeq \frac{4}{3} \gamma^2 \epsilon_{\text{CMB}}, \quad (26)$$

where ϵ_{CMB} is a characteristic CMB photon energy. For $E_{\text{IC}} = 0.3-10 \text{ keV}$, this corresponds to $\gamma \sim 6 \times 10^2-$

3.5×10^3 , which radiate synchrotron emission at

$$\nu_{\text{syn}} \simeq \frac{3eB}{4\pi m_e c} \gamma^2 \approx 4.2 \text{ MHz} \left(\frac{B}{1\mu\text{G}} \right) \left(\frac{\gamma}{10^3} \right)^2. \quad (27)$$

Thus, for $B \sim 1 \mu\text{G}$, the electrons relevant for 0.3–10 keV IC emission correspond to synchrotron frequencies of order $\nu_{\text{syn}} \sim$ a few–50 MHz, below the commonly observed ~ 100 –200 MHz bands. For an order-of-magnitude estimate we therefore (i) anchor the normalization to the measured integrated flux density at $\nu \simeq 150$ MHz for the Toothbrush relic and (ii) assume that the low-frequency spectrum is not strongly curved, so that νS_ν does not vary by more than an order of magnitude across the relevant MHz range (e.g., for $\alpha \simeq 1$, $\nu S_\nu \propto \nu^{1-\alpha} \approx \text{const}$).

Adopting S_{150} for the Toothbrush relic, which implies $\nu S_\nu \sim$ a few $\times 10^{-15}$ erg cm $^{-2}$ s $^{-1}$, and using $z \simeq 0.3$ (so that $B_{\text{CMB}} \simeq 3.25(1+z)^2 \simeq 5.5 \mu\text{G}$), we obtain a characteristic IC energy flux $EFE \sim (U_{\text{CMB}}/U_B) \nu S_\nu \sim$ a few $\times 10^{-14}$ erg cm $^{-2}$ s $^{-1}$ for $B \sim 2 \mu\text{G}$. Suzaku observations of the Toothbrush relic region report a non-thermal inverse-Compton upper limit of 2.4×10^{-13} erg cm $^{-2}$ s $^{-1}$ in the 0.3–10 keV band, implying a lower bound on the magnetic field strength of $B \gtrsim 1.6 \mu\text{G}$ [48]. This constraint is consistent with our radio-normalized order-of-magnitude estimate.

VI. SUMMARY AND DISCUSSION

In this work, we have examined ballistic surfing acceleration (BSA) as a mechanism for producing relativistic electrons in galaxy cluster merger shocks and powering radio relic emission. Our results demonstrate that BSA is a physically viable acceleration channel under cluster conditions characterized by low Mach numbers, weak magnetic fields, and uncertain turbulence. Because BSA is governed by large-scale shock electrodynamics, it can operate efficiently where multiple acceleration mechanisms may coexist.

By balancing coherent acceleration by the convection electric field against radiative losses, we find that BSA can accelerate electrons to Lorentz factors $\gamma \sim 10^4$ – 10^5 under plausible cluster conditions. The resulting steady-state electron distributions naturally exhibit high-energy steepening and spectral curvature, producing synchrotron spectra broadly consistent with observed radio relics. These results indicate that spectral curvature and high-frequency cutoffs in radio relics may arise directly from the interplay between coherent acceleration and radiative cooling, providing a probe of shock electrodynamics in the intracluster medium.

Although uncertainties remain regarding the detailed efficiency of the process, encapsulated in the effective parameter η_{BSA} , the small values inferred from observations are physically plausible and sufficient to generate the required electron energies owing to the energy-independent acceleration rate of BSA. Overall, our findings identify BSA as a promising contributor to electron energization in galaxy cluster merger shocks and highlight radio relics as key environments for testing coherent acceleration mechanisms.

[1] R. J. van Weeren, H. J. A. Röttgering, M. Brüggen, and M. Hoeft, *Science* **330**, 347 (2010), arXiv:1010.4306 [astro-ph.CO].

[2] M. Brüggen, A. Bykov, D. Ryu, and H. Röttgering, *Space Science Reviews* **166**, 187 (2012), arXiv:1107.5223 [astro-ph.HE].

[3] A. Stroe, T. Shimwell, C. Rumsey, R. van Weeren, M. Kierdorf, J. Donnert, T. W. Jones, H. J. A. Röttgering, M. Hoeft, C. Rodríguez-Gonzálvez, J. J. Harwood, and R. D. E. Saunders, *Monthly Notices of the Royal Astronomical Society* **455**, 2402 (2015), <https://academic.oup.com/mnras/article-pdf/455/3/2402/9382723/stv2472.pdf>.

[4] R. J. van Weeren, F. Andrade-Santos, W. A. Dawson, N. Golovich, D. V. Lal, H. Kang, D. Ryu, M. Brüggen, G. A. Ogrean, W. R. Forman, C. Jones, V. M. Placco, R. M. Santucci, D. Wittman, M. J. Jee, R. P. Kraft, D. Sobral, A. Stroe, and K. Fogarty, *Nature Astronomy* **1**, 0005 (2017), arXiv:1701.01439 [astro-ph.HE].

[5] R. J. van Weeren, F. de Gasperin, H. Akamatsu, M. Brüggen, L. Feretti, H. Kang, A. Stroe, and F. Zandanel, *Space Science Reviews* **215**, 16 (2019), arXiv:1901.04496.

[6] Rajpurohit, K., Wittor, D., van Weeren, R. J., Vazza, F., Hoeft, M., Rudnick, L., Locatelli, N., and et. al., *Astronomy & Astrophysics* **646**, A56 (2021).

[7] M. Hoeft and M. Brüggen, *Monthly Notices of the Royal Astronomical Society* **375**, 77 (2007), <https://academic.oup.com/mnras/article-pdf/375/1/77/3089639/mnras0375-0077.pdf>.

[8] G. Siemieniec-Ozieblo and B. Pasternak, *Astronomische Nachrichten* **332**, 649 (2011).

[9] A. Pinzke, S. P. Oh, and C. Pfrommer, *Monthly Notices of the Royal Astronomical Society* **435**, 1061 (2013), arXiv:1301.5644 [astro-ph.CO].

[10] A. R. Bell, *Monthly Notices of the Royal Astronomical Society* **182**, 147 (1978).

[11] R. D. Blandford and J. P. Ostriker, *The Astrophysical Journal Letters* **221**, L29 (1978).

[12] L. O. Drury, *Reports on Progress in Physics* **46**, 973 (1983).

[13] H. Kang and D. Ryu, *The Astrophysical Journal* **764**, 95 (2013), arXiv:1212.3246 [astro-ph.HE].

[14] D. Ryu, H. Kang, and J.-H. Ha, *The Astrophysical Journal* **859**, 102 (2018), arXiv:1711.06000 [astro-ph.HE].

nal **883**, 60 (2019), arXiv:1905.04476 [astro-ph.HE].

[15] H. Kang, D. Ryu, and J.-H. Ha, The Astrophysical Journal **876**, 79 (2019), arXiv:1901.04173 [astro-ph.HE].

[16] J.-H. Ha, S. Kim, D. Ryu, and H. Kang, The Astrophysical Journal **915**, 18 (2021).

[17] J.-H. Ha, D. Ryu, H. Kang, and S. Kim, The Astrophysical Journal **925**, 88 (2022).

[18] Y. Fujita, M. Takizawa, R. Yamazaki, H. Akamatsu, and H. Ohno, The Astrophysical Journal **815**, 116 (2015), arXiv:1511.01897 [astro-ph.HE].

[19] Domínguez-Fernández, P., Ryu, D., and Kang, H., Astronomy & Astrophysics **685**, A68 (2024).

[20] H. Kang and D. Ryu, The Astrophysical Journal **734**, 18 (2011), arXiv:1102.2561 [astro-ph.CO].

[21] H. Kang, D. Ryu, and T. W. Jones, The Astrophysical Journal **756**, 97 (2012), arXiv:1205.1895 [astro-ph.HE].

[22] L. Feretti, G. Giovannini, F. Govoni, and M. Murgia, The Astronomy and Astrophysics Review **20**, 54 (2012), arXiv:1205.1919 [astro-ph.CO].

[23] K. Stasiewicz, Physics **7**, 10.3390/physics7040051 (2025).

[24] D. Wittor, F. Vazza, and M. Brüggen, Monthly Notices of the Royal Astronomical Society **464**, 4448 (2016), <https://academic.oup.com/mnras/article-pdf/464/4/4448/8313677/stw2631.pdf>.

[25] S. Banfi, F. Vazza, and D. Wittor, Monthly Notices of the Royal Astronomical Society **496**, 3648 (2020), <https://academic.oup.com/mnras/article-pdf/496/3/3648/33485376/staa1810.pdf>.

[26] J.-H. Ha, D. Ryu, and H. Kang, The Astrophysical Journal **892**, 86 (2020), arXiv:1910.02429 [astro-ph.HE].

[27] S. Roh, D. Ryu, H. Kang, S. Ha, and H. Jang, The Astrophysical Journal **883**, 138 (2019).

[28] K. Stasiewicz and B. Eliasson, MNRAS **520**, 3238 (2023).

[29] K. Stasiewicz, MNRAS **524**, L50 (2023).

[30] K. Stasiewicz, MNRAS **527**, L71 (2023).

[31] T. P. Armstrong, M. E. Pesses, and R. B. Decker, Geophysical Monograph Series **35**, 271 (1985).

[32] R. B. Decker and L. Vlahos, Journal of Geophysical Research: Space Physics **90**, 47 (1985).

[33] T. Katou and T. Amano, The Astrophysical Journal **874**, 119 (2019).

[34] C. L. Sarazin, Reviews of Modern Physics **58**, 1 (1986).

[35] G. M. Voit, Reviews of Modern Physics **77**, 207 (2005), arXiv:astro-ph/0410173 [astro-ph].

[36] D. Eckert, F. Vazza, S. Ettori, S. Molendi, D. Nagai, E. T. Lau, M. Roncarelli, M. Rossetti, S. L. Snowden, and F. Gastaldello, Astronomy & Astrophysics **541**, A57 (2012), arXiv:1111.0020 [astro-ph.CO].

[37] M. Markevitch and A. Vikhlinin, Physics Reports **443**, 1 (2007), arXiv:astro-ph/0701821 [astro-ph].

[38] Murgia, M., Govoni, F., Feretti, L., Giovannini, G., Dallacasa, D., Fanti, R., Taylor, G. B., and Dolag, K., Astronomy & Astrophysics **424**, 429 (2004).

[39] F. Miniati, D. Ryu, H. Kang, and T. W. Jones, The Astrophysical Journal **559**, 59 (2001).

[40] D. Ryu, H. Kang, E. Hallman, and T. W. Jones, The Astrophysical Journal **593**, 599 (2003).

[41] F. Vazza, G. Brunetti, and C. Gheller, Monthly Notices of the Royal Astronomical Society **395**, 1333 (2009), <https://academic.oup.com/mnras/article-pdf/395/3/1333/18233401/mnras0395-1333.pdf>.

[42] J.-H. Ha, D. Ryu, and H. Kang, The Astrophysical Journal **857**, 26 (2018).

[43] G. M. Webb, L. O. Drury, and P. Biermann, Astronomy & Astrophysics **137**, 185 (1984).

[44] C. L. Sarazin, The Astrophysical Journal **520**, 529 (1999).

[45] G. B. Rybicki and A. P. Lightman, *Radiative processes in astrophysics* (1979).

[46] M. P. van Haarlem, M. W. Wise, A. W. Gunst, G. Heald, J. P. McKean, J. W. T. Hessels, A. G. de Bruyn, and et. al., Astronomy & Astrophysics **556**, A2 (2013), arXiv:1305.3550 [astro-ph.IM].

[47] R. Perley, P. Napier, J. Jackson, B. Butler, B. Carlson, D. Fort, P. Dewdney, B. Clark, R. Hayward, S. Durand, M. Revnell, and M. McKinnon, IEEE Proceedings **97**, 1448 (2009), arXiv:0909.1585 [astro-ph.IM].

[48] M. Itahana, M. Takizawa, H. Akamatsu, T. Ohashi, Y. Ishisaki, H. Kawahara, and R. J. van Weeren, Publications of the Astronomical Society of Japan **67**, 113 (2015).